Research Article | Vol. 14, No. 12 / 1 Dec 2023 / Biomedical Optics Express 6361
Biomedical Optics EXPRESS

Tailored photoacoustic apertures with superimposed optical holograms

GLENN A. HOWE,[1,2,3] MENG-XING TANG,[1] AND CHRISTOPHER J. ROWLANDS[1]

[1] *Department of Bioengineering, Imperial College London, Royal School of Mines, Prince Consort Road, London, SW7 2BX, UK*
[2] *g.howe@imperial.ac.uk*
[3] *glennhowe.ma@gmail.com*

Abstract: A new method of generating potentially arbitrary photoacoustic wavefronts with optical holograms is presented. This method uses nanosecond laser pulses at 1064 nm that are split into four time-delayed components by means of a configurable multipass optical delay apparatus, which serves to map the pulses onto phase-delayed regions of a given acoustic wavefront. A single spatial light modulator generates separate holograms for each component, which are imaged onto a photoacoustic transducer comprised of a thermoelastic polymer. As a proof of concept of the broader arbitrary wavefront construction technique, the spatially- and temporally-modulated holograms in this study produce a phased array effect that enables beam steering of the resulting acoustic pulse. For a first experimental demonstration of the method, as verified by simulation, the acoustic beam is steered in four directions by around 5 degrees.

Published by Optica Publishing Group under the terms of the Creative Commons Attribution 4.0 License. Further distribution of this work must maintain attribution to the author(s) and the published article's title, journal citation, and DOI.

1. Introduction

Ultrasound has been an invaluable tool for medical imaging for decades, and the properties of which have been studied extensively [1–3]. However, even as enlightening as the modality has proven to be, there exist numerous limitations such as the static configuration and number of transducer elements [2,4,5], and operator nuances leading to potentially inaccurate or inconsistent measurements [6,7]. Furthermore, conventional ultrasound transducers are typically arrays of elements numbering on the order of hundreds for linear arrays to thousands for 2D arrays [2,5]. This is orders of magnitude smaller than the number of elements in typical optical imaging systems, which commonly employ megapixel-scale resolutions.

Since photoacoustics introduces an optical-to-acoustic process regarding the generation of the ultrasound pulse [8–10], especially in the case of using laser pulses to irradiate a thermoelastic polymer, this modality employs some flexibility not seen in traditional ultrasonics. Photoacoustic ultrasound owes this flexibility to the fact that the transducer 'elements' can be arbitrarily arranged in both shape and number due to the optically-based nature of the irradiation patterns. Indeed, a photoacoustic transducer can theoretically approach a continuous 'array', much like how an optical aperture can be considered continuous. Careful modulation of both the temporal and spatial extent of this irradiation, as described in this study, can lead to wide ranging versatility of acoustic wave generation, resulting in photoacoustic spatial ultrasound modulation –conceptually a configurable acoustic phased array.

To produce high-fidelity optical patterns comprising the high-resolution photoacoustic aperture, the incident light is first modulated by refractive, diffractive, or other optical methods. While this may be done by physical elements [11,12], this technique is largely inflexible since the patterns are static. The use of patterned holograms, by means of spatial light modulators (SLMs), has also shown to be an effective method of modifying acoustic wavefront propagation [13–16], however

#507453 https://doi.org/10.1364/BOE.507453
Journal © 2023 Received 6 Oct 2023; revised 8 Nov 2023; accepted 10 Nov 2023; published 20 Nov 2023

Biomedical Optics EXPRESS

this relies on large illumination footprints and often necessitates the use of many acoustic cycles, thus eliminating the axial resolution benefits of single-oscillation pulses.

Photoacoustic phase modulation can be carried out by temporal modulation of the incident laser pulses. Previous implementations have used free-space [10,17] or fiber-based delivery [18–28], however these methods typically produce static linear phased arrays which are fixed in both number and size. Acoustic phase variation can also be achieved by the use of acoustic lenses which, analogous to optical lenses, directly modulate the incident acoustic pulse [29–36]. However, these are also static and inflexible in modulating the resulting acoustic wavefront.

Phase control in the photoacoustic aperture plane can alternatively be achieved by mapping the time delay of the incident laser pulses onto the phase delay of the resulting acoustic pulse. In this method, shown below, the acoustic phase is constructed by overlapping the optical patterns of different laser pulses with appropriate intensities, yielding a smooth phase gradient as shown in Fig. 1. The spatial and temporal modulations of the incident optical energy therefore manifest as an arbitrarily-patterned, 2D pulsed phased array.

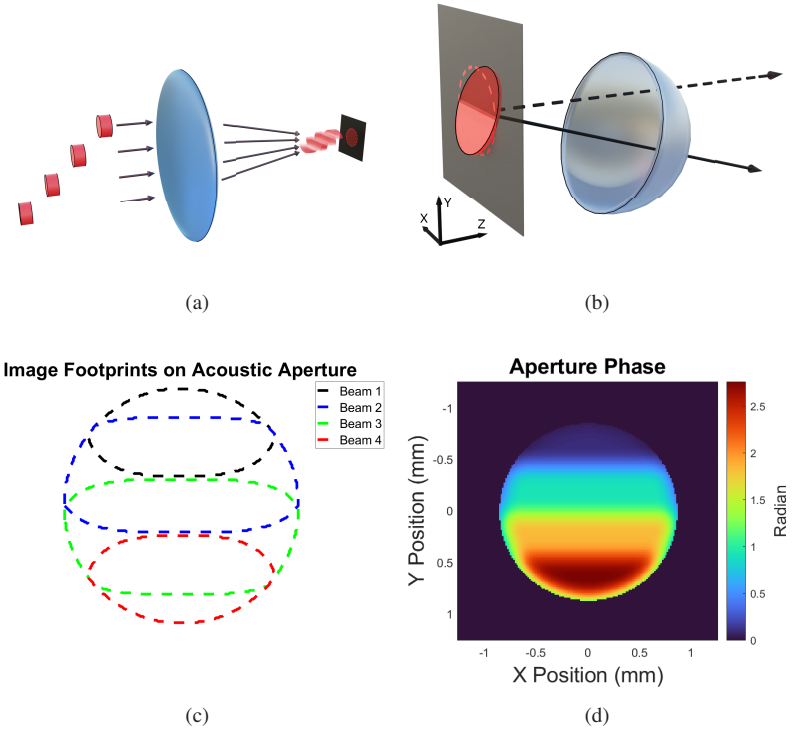


Fig. 1. Working principle of the instrument. **(a)** Four time-delayed laser pulses are imaged onto a thermoelastic polymer, creating an acoustic pulse. **(b)** The time delay acts as an acoustic phase delay, resulting in steerable wavefront propagation. **(c)** The optical patterns are modulated and overlapped in such a way that they result in **(d)** a continuous phase ramp across the photoacoustic aperture due to the smooth intensity transitions between individual beam components.

1.1. Scope and goals of subsequent investigation

By irradiating a thermoelastic polymer with spatially-overlapped, time-delayed holograms, a single laser-generated ultrasound (LGU) pulse is created whose wavefront is determined by the nature of the composite hologram image. This technique serves as an extension of traditional

Biomedical Optics EXPRESS

ultrasound by enabling greater flexibility and control over the extent and arrangement of the transducer 'elements', thus generating a wide variety of ultrasound wavefront morphology.

This study seeks to validate the aforementioned acoustic pulse generation concept. As a step towards building an arbitrary acoustic phase in the aperture plane, this approach used four time-delayed pulses to modulate the phase of an acoustic wavefront. A thermoelastic polymer consisting of polydimethylsiloxane (PDMS) and carbon black (CB) was used as a photoacoustic transducer which was irradiated by multiple time-delayed holograms. The holograms, when combined spatially, form an optically-driven acoustic phased array which has the flexibility of creating a wide range of photoacoustic apertures. A proof of concept demonstration of this wavefront generation technique, here in the form of a smooth phase gradient facilitating simple beam steering, is described below. The design of the optical delay line and description of the experimental setup is provided in Sec. 2, a simulation of expected results is described in Sec. 3, and the experimental results are shown in Sec. 4. A discussion of the results can be found in Sec. 5.

2. Methods

2.1. Experimental setup

Described below is the experimental setup with major components described in detail in their own subsection. The working principle of the instrument is illustrated in Fig. 1. Four time-delayed laser pulses, previously patterned by an SLM, were imaged onto a thermoelastic polymer. These SLM patterns, located at the pupil plane of the imaging system, carry optical phase modulations (holograms) that manifest as intensity distributions at the conjugate image plane (i.e. optical images on the photoacoustic transducer). The time-delayed pulses map to acoustic phase delays and therefore steer the resulting acoustic pulse away from normal incidence. The SLM-generated illumination patterns were overlapped in such a manner that the resulting phase ramp in the acoustic aperture is smooth and continuous.

The experimental setup is illustrated in Fig. 2. A nanosecond laser (Litron Nano-L 200-30) emits a single 6 ns, 1064 nm pulse and is immediately expanded from 1 mm diameter to 6.5 mm diameter. This expanded, collimated pulse was then injected into a combined beam splitter/beam delay apparatus which simultaneously splits the single pulse into four components and delays them temporally in succession (Sec. 2.2). These four temporally-delayed pulses were then collinearly aligned in a rectangular pattern before being directed onto the surface of an SLM (Sec. 2.3). The SLM operates on the four pulses independently to produce four distinct diffraction patterns –one for each time-delayed pulse. Still collinearly-aligned, these four diffraction patterns were then imaged onto the surface of a 'photoacoustic transducer' which is comprised of a composite thermoelastic polymer (Sec. 2.4).

The temporally-delayed patterns (images of the SLM Fourier space) act as sources of laser-generated acoustic pulses, and the time delays of the laser pulses map to the phase of the resulting acoustic pulses. These phase-delayed pulses are used to shape and steer the constructed acoustic wavefront, analogous to a conventional phased array [37]. Measurements of the acoustic wave were captured by a needle hydrophone which raster scans the plane orthogonal to the acoustic wave propagation direction to generate XY slices of the acoustic environment. As this is a proof of concept demonstration, the use of water, with its similar propagation characteristics to many biological tissues, was deemed sufficient for a first-order verification procedure.

2.2. Optical beam delay

Separating the initial single laser pulse into four was achieved by means of a custom optical delay line. The optical delay apparatus serves to both split the initial laser pulse into four roughly-equal-intensity components as well as to impart a sequential time delay between them as

Biomedical Optics EXPRESS

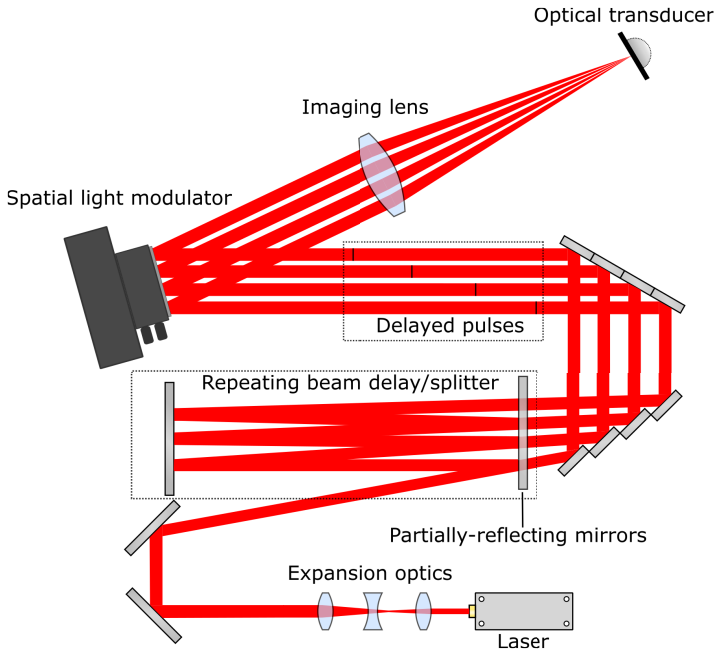


Fig. 2. Optical diagram of experimental setup. A single laser pulse is injected into a multipass optical splitter/delay line. The four time-delayed pulses are patterned by a spatial light modulator before being imaged onto a thermoelastic polymer which acts as a photoacoustic transducer. Note that the four beams are collinearly arranged in a rectangular pattern, but shown here in a line for illustrative purposes.

they propagate through the device. Seeing as the temporal delay of the laser pulses map to phase delays of the acoustic pulses, and considering the rapid speed of light, a considerable physical distance is required which necessitated the construction of a custom design. The design uses numerous mirrors to contain the pulses in a multipass loop which allows for a compact footprint while still achieving a large total temporal delay.

The design shares some principles with conventional multipass cells such as the White [38] and Herriot [39] cells in that a beam is temporarily trapped within a reflective cavity. This design, however, uses a number of partially-reflecting mirrors to allow the passage of a controlled amount of light at regularly-spaced intervals. Furthermore, this design allows for a wide range of delays (after reconfiguration and realignment) due to the usage of only flat mirrors. A free-space design was opted for as opposed to a fiber-based design due to considerations relating to both ease of delay tunability as well as laser induced damage when dealing with high power densities.

A render of the beam delay design is shown in Fig. 3(a). The small mirrors in the octagonal arrangement are relayed to other small mirrors in succession by means of the larger mirrors. Top-down beam paths for the first two passes are shown in Figs. 3(b) and 3(c). The green highlight shows the start of each pass while the red highlight shows the end, with some light escaping during each pass at the small, partially-reflective mirrors in the center. While the device can utilize a total of eight partially-reflecting mirrors, this study used only four beam components. The partially reflecting mirrors consist of a single Thorlabs BST05 (70:30 R:T) and two Thorlabs BSW05 (50:50 R:T). Considering the reflection percentages of the partially-reflective mirrors along with optical loses on each surface, the resulting pulse intensities at the output of the device are roughly 30%, 21%, 24%, and 24% of the initial pulse, respectively. Seeing as the use of an

Biomedical Optics EXPRESS

SLM can regulate the intensities of the four pulses independently in numerous ways (diffraction efficiency, coupling, etc.), this was taken as an acceptable first-order intensity regulation method.

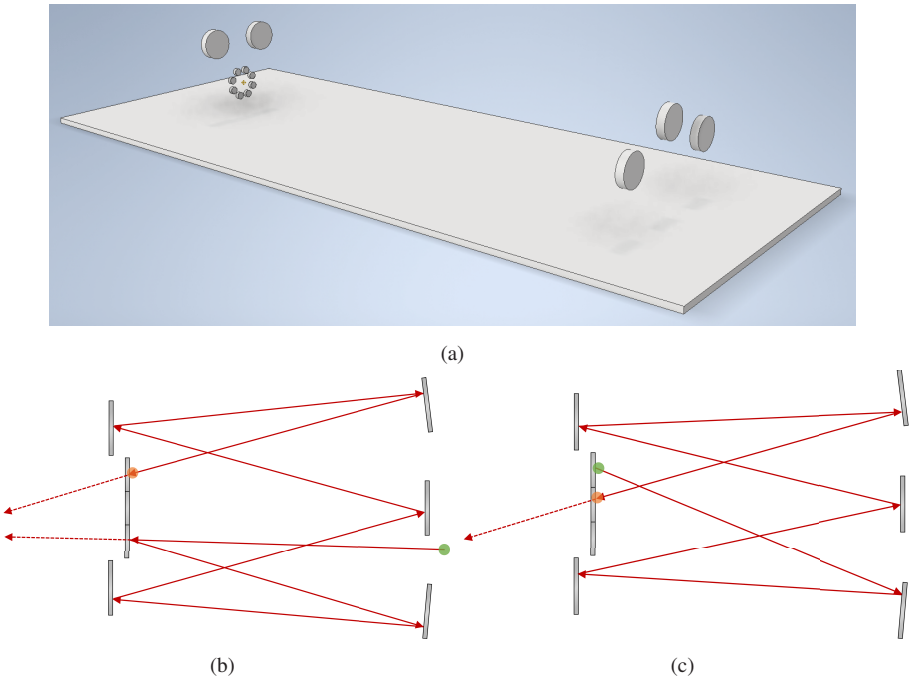


Fig. 3. The custom optical delay design. **(a)** shows a rendering of the optics (mounts and supports not shown), while **(b)** and **(c)** show the first two beam path loops, respectively. The start of each loop is highlighted in green while the end is highlighted in red. The small mirrors on the left side are partially-reflective, allowing some light to escape on each pass. This design is more configurable than other multipass cells in that the mirrors can be translated and realigned to modify the total time delay.

2.3. SLM hologram generation

Optical pattern generation was carried out via an SLM operating in phase-only mode (Meadowlark HSP1920-500-1200-HSP8). The face of the SLM has a resolution of 1920 x 1152 with a pixel pitch of 9.2 x 9.2 μm. After being temporally-delayed, the four laser pulses were then collinearly aligned in a rectangular pattern which corresponds to four quadrants of the SLM surface, as shown in Fig. 4(a). These four quadrants are controlled independently to create four distinct patterns.

Pattern generation was carried out by implementing a Gerchberg-Saxton (GS) routine. This is a simple, iterative phase retrieval method which quickly calculates the phase pattern necessary to produce a resulting target image given a known input illumination pattern [40]. For the experiments described here, the GS patterns were calculated and applied to the SLM quadrants prior to data collection, as exemplified in Fig. 4(b).

These SLM patterns, along with a blazed grating pattern, allow arbitrary images to be created free of contamination of zero-order diffraction effects. A lens captured the non-zero-order, phase-modulated light and produced the resulting images at the conjugate image plane of the SLM –the surface of the photoacoustic transducer. These images are four temporally-delayed components which were used to construct and shape an acoustic wavefront.

Biomedical Optics EXPRESS

2.4. Photoacoustic transducer

The construction and properties of non-biological optical transducers vary greatly in absorption efficiency, bandwidth, and ease of fabrication [41–52]. The photoacoustic transducer used in this study was a composite thermoelastic polymer comprised of PDMS and carbon black. Both materials are safe to use, easy to work with, and widely available. The aforementioned studies have investigated the use of similar composites and much work has been done to increase the bandwidth and optical absorption efficiency. Achieving high bandwidth was not a priority in this study. In fact, due to the relationship with the optical delay and acoustic phase, a lower bandwidth is advantageous. Furthermore, due to both the scope of this study and the large overhead in available laser power, maximizing optical absorption was also not a priority.

2.5. Needle hydrophone

To capture the resulting acoustic field generated from the incident laser pulses on the photoacoustic transducer, a needle hydrophone was employed (Precision Acoustics 0.5 mm (NHO500)). This particular device has a working frequency range of 0.2–40 MHz with a typical ±4dB response in the 1–20 MHz range.

Scanning motion of the needle hydrophone was carried out by a microscope stage (Prior Scientific H101A). Its large range of motion (114 x 75 mm) and small step size (0.01 μm) allows both flexibility and repeatability. The stage was oriented vertically enabling lateral, 2D slices of the acoustic field. The hydrophone was affixed to the stage via a custom plate adapter and mounting hardware. Z-axis control was handled by Thorlabs LT1 2-inch manual translation stage.

2.6. Data acquisition

Signals captured from the needle hydrophone were recorded and digitized by a two-channel oscilloscope (Redpitaya STEMlab 125-14). Running at a sampling rate of 125 MHz with a bit depth of 14, the first channel captured the Q-switch trigger signal from the laser while the second channel captured the acoustic signal from the needle hydrophone. A home-built script written in Python handled the collection, parsing, and organization of each measurement while also commanding the vertically-oriented microscope stage to scan a 2D slice of acoustic environment.

3. Simulation of expected results

3.1. Simulation methods

Traditional phased array wavefront propagation including beam steering and arbitrary wavefront generation can be modeled via simple methods stemming from Huygen's Principle of wavefront propagation. The Rayleigh-Sommerfeld diffraction (RSD) equation (Eqn. 1) describes the field $u(x, y; z)$ at some downstream z location given the field $u_0(s, t)$ at the initial propagation point (z_0):

$$u(x, y; z) = \frac{1}{\lambda} \iint_{P_0} u_0(s, t) \left[\frac{1}{\kappa r} - i \right] \frac{z e^{i\kappa r + \phi(s,t)}}{r^2} \, dsdt \tag{1}$$

where $r = \sqrt{(x-s)^2 + (y-t)^2 + z^2}$, $\kappa = \frac{\lambda}{2\pi}$, P_0 is the 2D region of the photoacoustic aperture, and $\phi(s, t)$ is the local phase offset. The arguments (s,t) and (x,y) describe lateral dimensions in the initial and resulting field, respectively.

While slow, RSD permits the interrogation of all planes of the propagation environment with a simple 'permutation' of the Cartesian variables. Furthermore, one may apply an additional envelope to the exponential term, thus permitting an interrogation of the acoustic pulse length. The additional envelope has consequences for beam steering and side lobe formation. While similar results, along with improvements in computation speed, can be achieved using the Angular

Biomedical Optics EXPRESS

Spectrum Method (ASM) and related techniques [53], the familiarity and flexibility of RSD propagation outweigh the speed benefits of ASM for this study. The simulations, and analysis thereof, were performed in MATLAB R2021b.

3.2. Simulation parameters

3.2.1. Time and phase delay

As described in Sec. 2.2, the sequential time delay between laser pulse components is 36 ns, corresponding to a total delay of 108 ns. Although this time delay is static, it naturally corresponds to different total phase delays for different acoustic pulse wavelengths. Unless stated otherwise, all results in this study map the 108 ns time delay to the given acoustic wavelength in question.

3.2.2. Photoacoustic aperture

The size of aperture has profound effect on the nature of wavefront formation and beam steering. Not only is diffractive beam spreading a function of aperture size, but also is the overall phase gradient (since the total time delay is constant), and therefore the degree to which a beam can be steered. Prior experimental investigations have guided this study to adopt a photoacoustic aperture diameter of 1.7 mm which has been shown to provide an acceptable optimization between beam spread and steering capabilities. This size regime also affords sufficient optical power density to facilitate an appreciable acoustic pulse amplitude. In other words, the incident SLM-generated laser patterns combine to form an image on the photoacoustic transducer with a total diameter of 1.7 mm.

3.2.3. Simulation dimensions

Prior experimental investigation had also shown the center frequency of the given thermoelastic polymer to be around 1–10 MHz (dependent upon construction methods and materials used), thus corresponding to a dominant wavelength of roughly 150–1500 μm when assuming a roughly 1500 m/s propagation speed in water. The simulation volume was then taken to be a cube with length of 20 mm which permits investigation of a wide range of transducer apertures while still being well within the Fraunhofer (far-field) regime [54]:

$$r_f > \frac{D^2}{4\lambda} \tag{2}$$

where D is the extent of the radiation source. This allows apertures to be maximally a few mm which is more than adequately large for the beam steering technique laid out in this study.

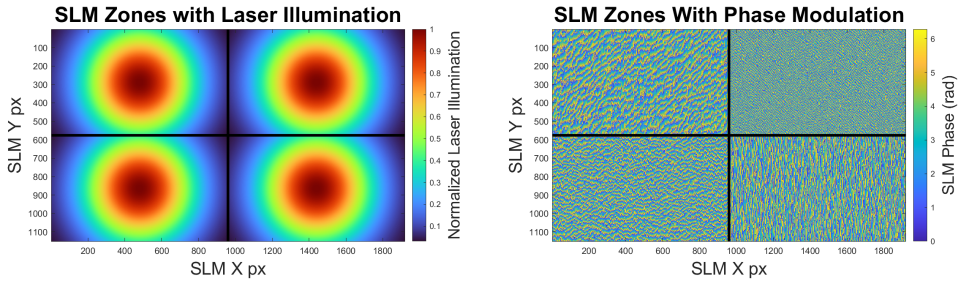
3.2.4. Simulation resolution

While the RSD method provides an exact solution at infinitesimal resolution elements [53], an arbitrarily large resolution often yields diminishing returns given the increase in computational expense. To optimize the efficiency and accuracy of the simulation, a given ‘beam forming feature’, in this case beam steering deviation, is measured vs. the simulation grid resolution elements. A simple 108 ns ’phase’ ramp was applied to an aperture 1.7 mm in diameter, and the resulting beam was propagated to a z distance of 20 mm. Deviations were measured via 2D Gaussian fits to the resulting XY acoustic amplitude profile. Figure 5 shows the results for three acoustic wavelengths spanning 1–10 MHz, highlighting the clear asymptotic trend in each case. Applying a simple power function fit to the data reveals a practical limit to the increase of resolution elements at around 1300 (corresponding to roughly $\lambda/10$ at 10 MHz), signifying a suitable value that will be used for the remainder of this study.

Biomedical Optics EXPRESS

3.3. Hologram generation

A diagram of the SLM surface with the locations of the four collinearly-aligned laser beams is shown in Fig. 4. The SLM contains pre-generated, Fourier-plane patterns which both shape the optical wavefront and also steer the light away from the zero-order diffraction angle. These GS patterns are calculated from the known incident intensity distribution and the intended image plane patterns. An optical lens facilitates the imaging of the four independent patterns simultaneously on a single image plane. Figure 6 shows the intended individual target patterns along with the overlapped pattern as seen by the photoacoustic transducer. Figure 7 shows a recorded image of the target hologram images. The images show a pattern approximately 7 mm in diameter for illustrative purposes, whereas the illumination patterns used in this investigation were 1.7 mm in diameter carrying a total fluence of 15.1 mJ/cm^2. Speckles are an inherent aspect of discrete hologram imaging, and can be exacerbated by small optical apertures (e.g. laser beam diameters) along with finite Fourier frequency components (e.g. divided SLM surface regions and non-unity SLM pixel fill factor). Furthermore, the GS routine used can converge to an 'exact' solution only in very rare or contrived circumstances; in the general case a degree of speckle is unavoidable, although minor improvements are possible with increased numbers of iterations. For the purposes of this proof of concept demonstration, the number of iterations were kept comparatively few for simplicity and time constraints. Improvements in efficiency in modifications to the GS routine are a current avenue of exploration, as is optimizing the optical imaging pathways to reduce the noise in the resulting images. The effect of the speckle pattern on the resulting acoustic wavefront is described in Sec. 4.2.



(a) (b)

Fig. 4. Diagrams of the **(a)** illumination and **(b)** example phase of the SLM surface. The four roughly-equal-intensity beams are collinearly aligned and are operated on by four distinct regions of the SLM surface, allowing for independent control over the four resulting diffraction patterns. The phases shown in (b) are example patterns generated by implementing a Gerchberg-Saxton routine (Section 2.3). The resulting intensity distributions, when imaged through the lens, are shown in Fig. 7.

3.4. Acoustic field propagation

The photoacoustic aperture intensity and phase distribution was propagated via RSD to a distance of 20 mm using the parameters laid out in the proceeding sections. The resulting XY cross section was downsampled to a resolution of 21 x 21 points, matching the sampling of the needle hydrophone. This acoustic field sampling resolution was found to be an acceptable optimization of data collection speed and wavefront recovery fidelity at the tolerances necessary for this study to confirm conceptual realization of the beam steering method.

Figure 8 shows the results from the RSD wavefront propagation. A flat wavefront at 10 MHz is first shown in Fig. 8(a) while Figs. 8(b) to 8(d) show steered beams with frequencies of 10,

Biomedical Optics EXPRESS

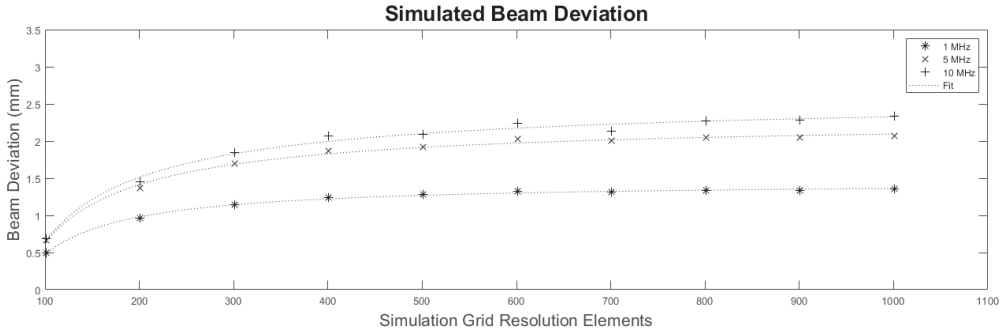


Fig. 5. Results of simulating beam steering at constant aperture phase ramp with different simulation resolutions and pulse frequencies. The beam deviations asymptote to 1.4, 2.2 and 2.5 mm for the 1, 5, and 10 MHz frequencies, respectively.

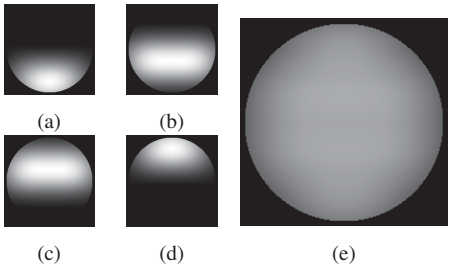


Fig. 6. Simulated images of the four SLM hologram patterns as seen by the photoacoustic transducer. When the separate beam patterns **(a-d)** overlap, the result is a complete circular disk **(e)**, thus maintaining an even illumination and smooth phase ramp across the aperture.

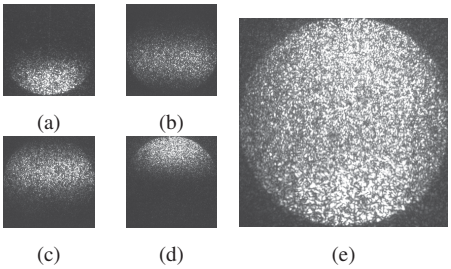


Fig. 7. Camera images of the four SLM hologram patterns as seen by the photoacoustic transducer. The individual patterns **(a-d)** were produced by the four separate regions of the SLM and imaged on the photoacoustic transducer. **(e)** shows the images overlapped simultaneously for illustrative purposes when in fact each pulse is sequentially time delayed by around 36 ns.

Biomedical Optics EXPRESS

5, and 1 MHz, respectively. The sub panels show, from left to right, the aperture phase, a full-resolution YZ lateral view of beam directionality, a polar plot of beam directionality, and the simulated, downsampled XY transverse hydrophone measurement. Aperture phases were calculated assuming a 108 ns total phase delay for the respective frequencies.

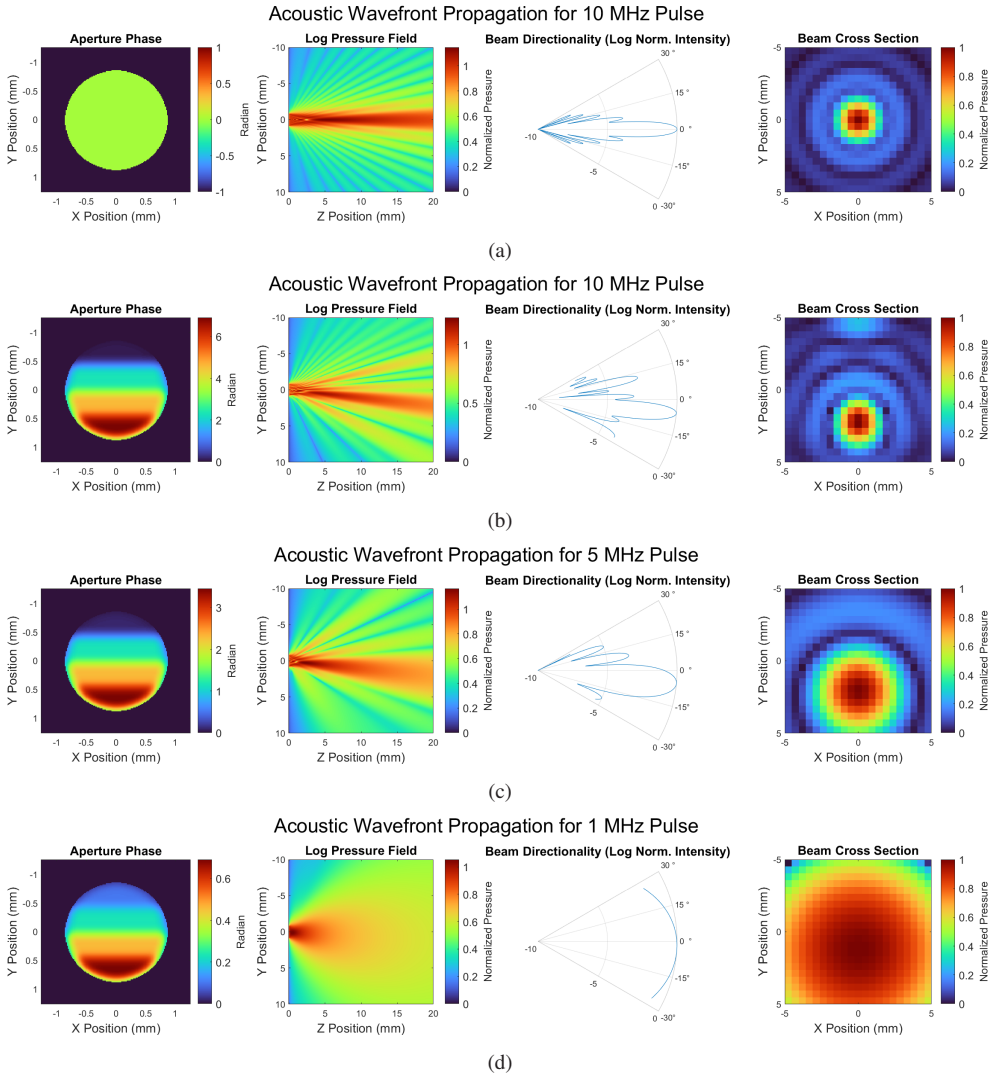


Fig. 8. Simulation results of the RSD propagation method for acoustic frequencies ranging from 1–10 MHz. **(a)** shows no beam steering while **(b)-(d)** show smooth phase ramps. In each of (a-d), from left to right, the first panel shows the phase ramp across the aperture, the second shows a YZ cross section (where Z is the propagation direction) of the resulting beam formation, the third shows a corresponding polar plot, and the last shows an XY pressure map at 20 mm. While the total delay was 108 ns for each simulation, this corresponds to different total acoustic phase ramps for different acoustic frequencies.

Biomedical Optics EXPRESS

4. Experimental results

4.1. Acoustic Pulses and Bandwidths

Synchronized times series of the four individual acoustic pulse components are shown in Fig. 9, corresponding to the illumination patterns shown in Fig. 7. Pulse intensity normalization was controlled by adjusting the independent diffraction efficiency of each beam within the separate SLM zones shown in Fig. 4. Still, inhomogeneities in the thermoelastic polymer can manifest as modulation of the pulse intensity, as is illustrated by the slightly larger amplitude in the first pulse component of the shown traces. Further discussion can be found in Sec. 5.1

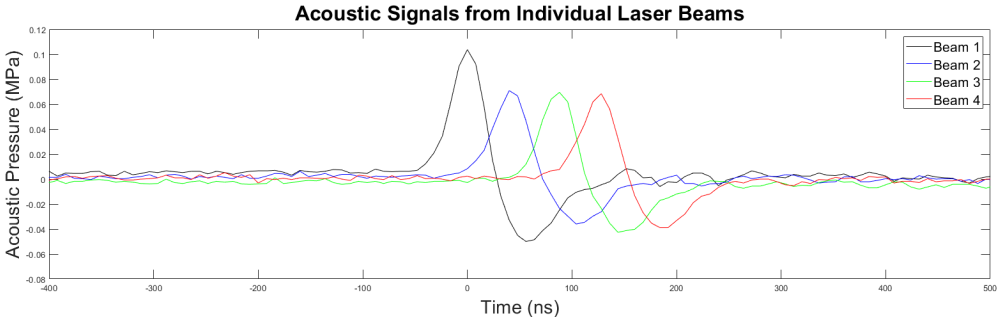


Fig. 9. Time series of typical acoustic pulses generated from the individual laser illumination pattern components, synchronized and overlapped. The sequential time delay is around 36 ns. The illumination patterns, as described in Sec. 2.3, spatially overlap in conjunction with the time delay to produce an even phase ramp. Intensity inhomogeneity is likely due to thermoelastic polymer features discussed in Sec. 5.

Previous experiments showed a typical frequency response to a PDMS+CB composite irradiated by a 6-ns 1064 laser to be between 1–10 MHz. For this investigation, the upper limit was targeted to provide adequate bandwidth for both single pulses and multi-component combined pulses which naturally stretch out the emergent pulse period and thus lowers the resulting frequency.

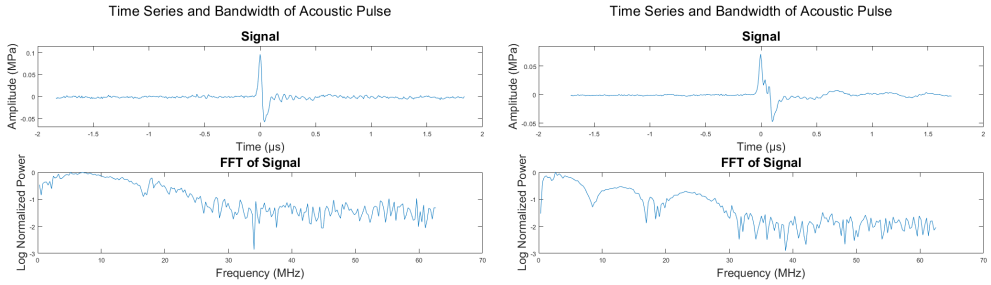
Figure 10(a) shows a time series and accompanying fast Fourier transform (FFT) of a sample acoustic pulse from a single laser pulse component. As expected, the central frequency lies around 10 MHz. Figure 10(b) shows similar results for a multi-component combined pulse. It is seen that the central bandwidth shifts towards lower frequencies accompanied by more structure at higher frequencies. This structure is not the governing characteristic of the bandwidth, therefore the dominant frequency is taken to be the maximally-represented frequency of around 4 MHz. The expected results for this particular photoacoustic transducer are assumed to carry a similar dominant frequency.

4.2. Measurement stability and uncertainty

Given that the morphology of the LGU pulse described in this study is dependent upon laser intensity –the resulting composite pulse being a specific combination of multiple phase components– modulations in laser output intensity may produce unwanted wavefront aberrations yielding erroneous beam propagation. To examine the stability and repeatability of the wavefront generation technique, the measurement uncertainty of both the laser output and needle hydrophone signal was quantified. A single component of the laser output, after expansion and collimation, was recorded on table top camera (iDS UI-3080CP-M-GL).

The X and Y widths were measured via 2D Gaussian fitting over the course of ~140 measurements, and have a normalized standard deviations, signified by the shaded region, of around 0.3% as shown in Figs. 11(a) and 11(b), respectively. Given that the optical beam is

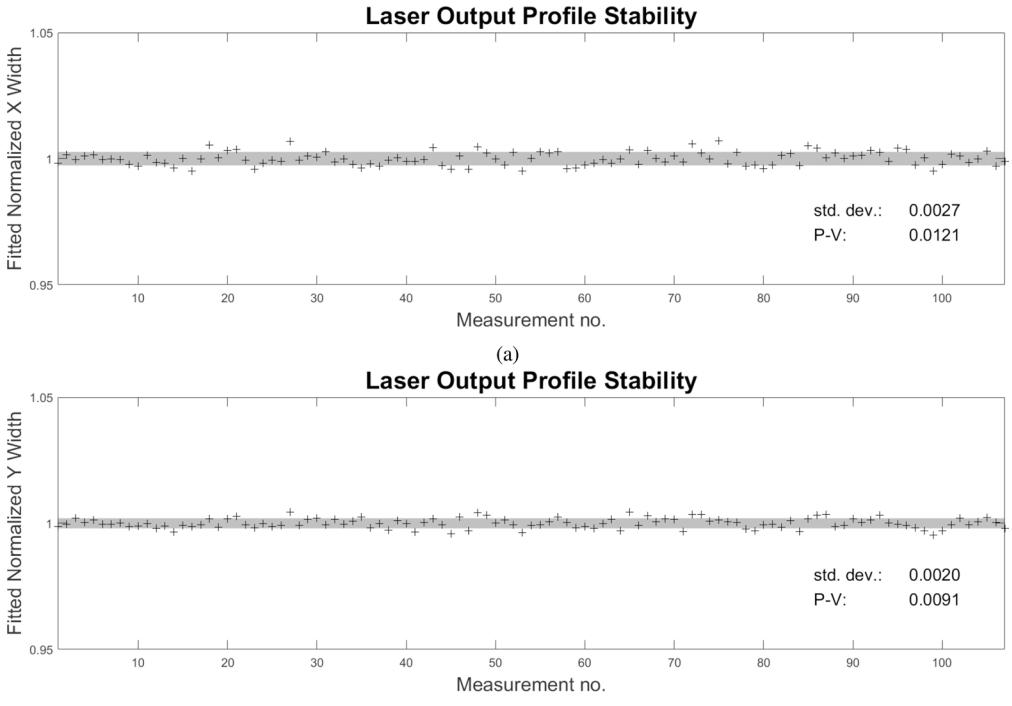
Biomedical Optics EXPRESS



(a) (b)

Fig. 10. Time series and FFT of examples of a typical **(a)** single and a **(b)** composite pulse. Having been constructed from multiple time-delayed pulses, the composite pulse naturally has a lower peak frequency (along with higher-order structure).

around 3 mm in radius, this corresponds to around 9 μm –or around 1 SLM pixel– in variation. While this small variation is assumed to by statistically insignificant for this current proof of concept (and therefore not modeled in the simulation), it will be a topic of investigation for future applications using more complicated acoustic wavefronts.



(a)

(b)

Fig. 11. Time series of 2D Gaussian fits to the laser output spatial profile showing the variation in the **(a)** X width, and **(b)** Y width. The measured standard deviation and peak to valley are displayed, showing spatial variation under 0.3%. The gray shaded area encompasses 1σ.

Figure 12(a) shows the normalized total optical signal produced by the beam over the span of ~140 measurements. The shaded area signifies the 1σ range of 0.0232 while the total

Biomedical Optics EXPRESS

peak-to-valley (P-V) distribution is .1066. Figure 12(b) shows the normalized measured signal from the stationary needle hydrophone while it recorded the acoustic wavefront generated from the aforementioned single laser component over the course of ~120 measurements. While the published uncertainties range from 9-18% over the working frequencies, the shaded area shows the 1σ range to be 0.0343 while the P-V distribution is 0.1960. Using the normalized mean and standard deviation from Figs. 12(a) and 12(b), the SNR of the optical images and resulting acoustic pulses are around 43 and 29, respectively.

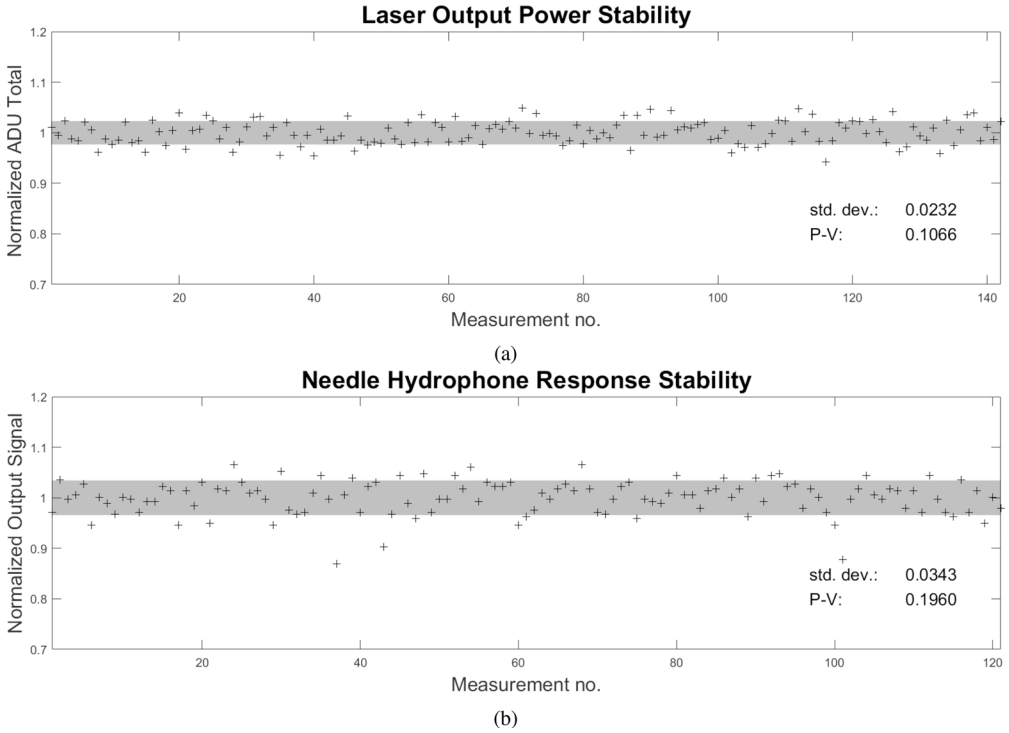


Fig. 12. Time series of measurement stability for the **(a)** laser output, and **(b)** needle hydrophone. The laser output was determined by summation of ADU of a single time-delayed beam component, while the needle hydrophone measured the acoustic signal from that same single time-delayed beam. The gray shaded area encompasses 1σ.

As our thermoelastic polymer composite behaves largely as a fixed-frequency transducer, the large variance in measurement uncertainties across appreciable bandwidth regions do not impact our ultrasound pulse generation method at this stage of development. Furthermore, the use of the needle hydrophone in this study serves only as a means to verify the ultrasound pulse generation technique. Future applications of the instrument (including clinical trials) will obviate the need for the needle hydrophone.

The effects of these systematic variations were modeled in two parts. First, a 2.3% Gaussian noise variation was added to the overall intensity of each simulated acoustic pulse. Since each hologram component is derived from a single laser pulse, each hologram component will vary in intensity identically resulting in an overall variation in the combined illumination pattern. A Gaussian noise distribution was also added to each needle hydrophone signal at the the resulting measurement plane. Although the needle hydrophone measurements contain within them the laser power variance, a worst-case scenario was assumed, and the combined propagated systematic measurement uncertainty was taken to be the combined uncertainty of around 5.7%. Second, a

Biomedical Optics EXPRESS

noise texture with similar spatial features as shown in Fig. 7 was applied to the intensities of each beam component before combination into the full composite pulse. This manifests as spatial noise in the overall phase profile (with an upper limit determined by the maximum phase delay). The propagation of this noisy wavefront was then simulated in identical fashion as described above.

An example of the simulated initial acoustic phase and resulting acoustic field is shown in Fig. 13. The noisy wavefront propagation simulation was run around 50 times and the fitted X and Y centroids of the final pulse deviation were recorded. The results of the centroid fitting are displayed in Fig. 14, showing a Y centroid displacement of 2.16 ±0.05 mm. Not shown is the X centroid deviation which has a similar variation around 0 mm.

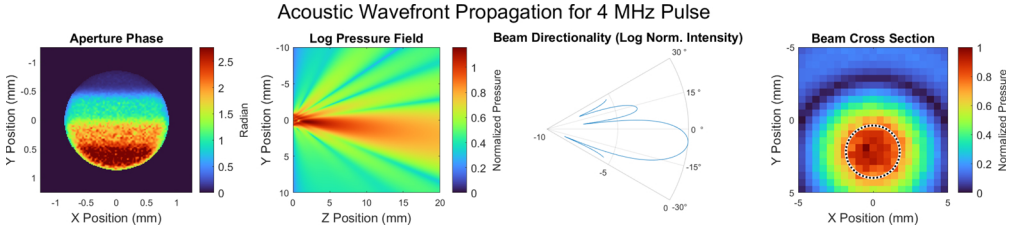


Fig. 13. An example of the effects of uncertainties in both laser output and needle hydrophone measurement. The noise morphology in the left panel follows the spatial extent of that shown in Fig. 7, and the right panel shows a simulated measurement from this propagated wavefront at the needle hydrophone.

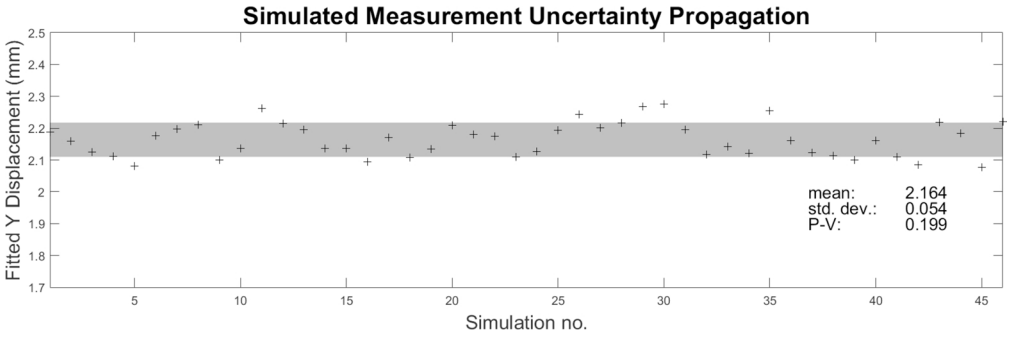


Fig. 14. Y centroid variation of final acoustic pulse with propagated uncertainties in laser output power and needle hydrophone measurement over the course of around 50 simulation runs. The fitted Y centroid of the resulting acoustic pulse is 2.16 ±0.05 mm (compared to 2.1 mm without uncertainty propagation). The gray shaded area encompasses 1σ.

4.3. Measured acoustic field

The results of the measured acoustic field are shown in Fig. 15. In the left-hand panels, which show the measured data, an obvious feature not captured by the simulation are the 'residuals' residing at the center of each acoustic field. While this feature is discussed in Sec. 5, it is here assumed to be distinct from the steered beams' amplitude. As such, a 2D Gaussian fit was applied to an exponential threshold of the measured acoustic field to isolate the steered beam from the residuals. These Gaussian fits are shown in the right-hand panels. The black dashed circles indicate the non-steered beam locations while the red dashed circles indicate the expected 2.16 mm deviations as given by the results of the RSD simulation. A summary of the beam

Biomedical Optics EXPRESS

steering results is presented in Table 1. This table shows the simulated and measured results of the (x, y) deviations for the four cardinal directions, with boldface numbers signifying the intended direction. Three of the four measurements fall within 90% of the expected deviation magnitudes, with minor angular deviations from the expected cardinal directions. The leftward steered beam saw roughly 50% expected deviation and strong zero-order residual.

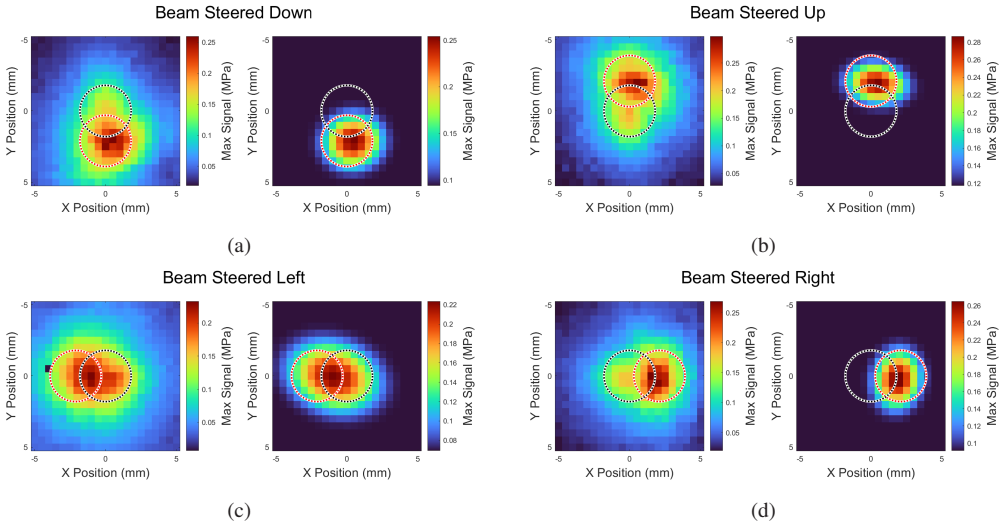


Fig. 15. Measured results from the photoacoustic phased array. In each subfigure, the left panel shows the recorded data while the right panel shows Gaussian fits applied to an exponential threshold of the measurements. The non-deviated locations are marked with a black dashed circle while the expected deviations are marked with a red dashed circle. (a), (b), and (d) show ~90% agreement with expected results while (c) shows ~50% agreement, likely due to thermoelastic polymer inhomogeneity.

Table 1. Measured beam steering with comparison to simulation. For each of the cardinal directions shown in this study, the (x, y) deviations in mm are displayed, with boldface numbers signifying the intended direction.

Method	Total Beam Shift (x, y) [mm]			
	Down	Up	Left	Right
Simulation	(0.0, **-2.16**)	(0.0, **2.16**)	(**-2.16**, 0.0)	(**2.16**, 0.0)
Measurement	(0.4, **-2.1**)	(0.4, **1.9**)	(**-0.9**, 0.1)	(**1.9**, 0.2)

As further verification of the beam steering technique, time series at two differing Y-axis locations are shown in Fig. 16(a). The earlier wavefront pixel shows a composite nature which is indicative of pulses arriving from the center of the photoacoustic aperture, while the latter wavefront pixel has a pulse profile corresponding to a single pulse component –namely due to the photoacoustic aperture component that is most delayed in phase. The red and blue time series correspond to the red and blue circles in Fig. 16(b) which shows the acoustic field and corresponding phase map, respectively.

Biomedical Optics EXPRESS

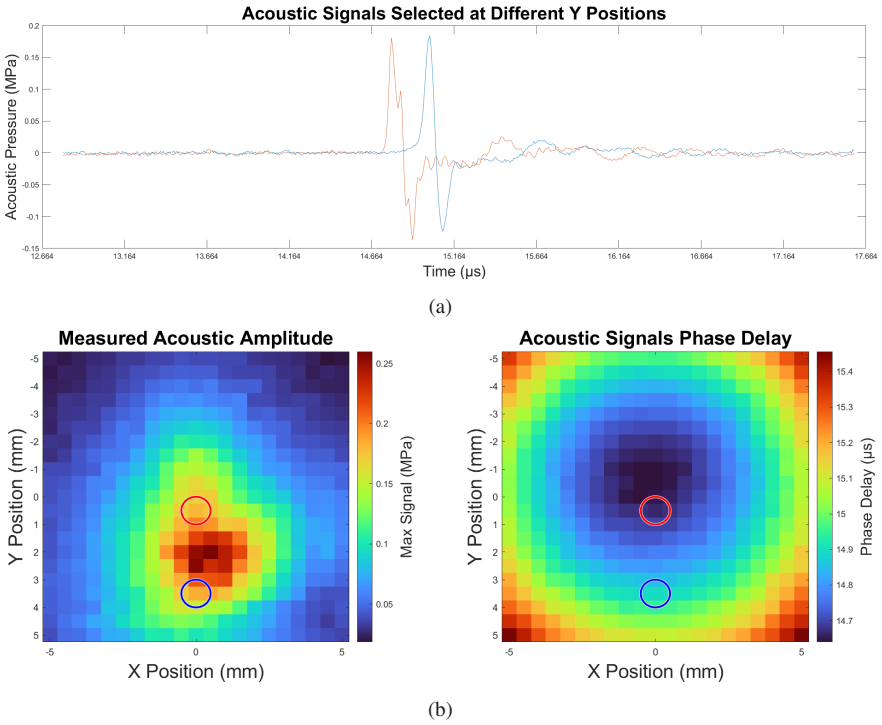


Fig. 16. **(a)** Time series of measurements at different Y positions, and **(b)** intensity and phase maps of the measured acoustic field. The red and blue traces in (a) were taken at the locations shown as red and blue circles in (b).

5. Discussion and conclusions

5.1. Remarks on experimental setup

The residuals, indicated in Sec. 4, have a few likely sources. First, due to the interferometric principles of a phased array, mismatches in pulse intensity will result in non-uniform destructive interference along non-steered directions. Second, highlighted by the asymmetric nature of the 4-direction beam steering shown in Fig. 15, the construction of the composite thermoelastic acoustic transducer led to inhomogeneities in optical absorption. While the circular illumination pattern (phase ramp) irradiated the same location on the transducer surface, the rotations in the azimuthal direction that is necessary for beam steering in different directions led to the four beam patterns falling on different regions of the circular area on the transducer surface. Furthermore, as shown in Fig. 10, the profiles of the acoustic pulse depend upon the number of combined hologram components that construct it –namely by increasing the period of the resulting pulse. This differentially affects the propagation of each composite pulse thus leading to nonuniform interference. Lastly, the surface of the transducer is not perfectly flat, and therefore the height variations manifest as phase variations leading to further deviations from ideal interference.

While a time delay can be accomplished via fiber coupling, this investigation chose to showcase the abilities of free-space optical delay. First, as is common when dealing with high power densities, the risk of laser induced damage is great concern –one which is mitigated in a free-space design. An obvious trade-off related to overall optical train alignment stability is apparent, however there exists a non-negligible freedom in pointing tolerance provided the vibrational and thermal environment is calm and invariable. A free-space design further permits easy access to beam modification at numerous points along the optical path. While not demonstrated in

Biomedical Optics EXPRESS

this study, intra-path beam modification can prove to be beneficial to maintain homogeneity in intensity, diameter, polarization, etc. Finally, a free-space design allows for straightforward tuning of the optical delay line without the need for new hardware. Realignment of the aforementioned optical delay apparatus is not trivial, however it is considerably less involved than replacing optics, fibers, hardware, etc.

5.2. Future of tailored acoustic wavefront generation

The overall extent to which beam steering can be accomplished by the phased array technique laid out in this study is largely dependent upon the amount of total photoacoustic phase delay available. While this study served as a demonstration of a wavefront generation technique by constructing a simple phase ramp, the possible extensions of the technique are far reaching. Indeed, with enough phase-delayed components, arbitrary phase maps can be constructed resulting in wavefront control analogous to optical techniques [55,56].

Prior testing of phase wrapping across the acoustic aperture, namely when utilizing a single oscillation, has shown to produce considerable artifacts and side lobes. Increasing the available phase delay to incorporate multiple oscillation cycles can foster even more flexibility in wavefront generation. These advancements are practical concerns, however, and are not theoretical limitations. Indeed, extensions of the method described in this study can yield conceptually arbitrary wavefront generation. Ongoing developments of this technique include increasing the total number of time-delayed optical holograms, therefore enabling a wider variety of acoustic wavefronts and will be the topic of future publications.

Further improvements upon the existing proof of concept are currently underway, including the homogenization of the thermoelastic polymer composite and speckle reduction of the optical holograms. These improvements will not only increase the stability and repeatability of the resulting ultrasound pulse, but will also enable finer spatial control over the acoustic wavefront, enabling higher order control that is required for target focusing and arbitrary wavefront propagation.

Additionally, patterning the light by means of an SLM affords much flexibility in spatial patterns, however the refresh rate of available devices lack the speed of traditional piezoelectric transducers. The SLM model used in this study was, at the time of purchase, the fastest high-order device readily available, with a refresh rate just under 300 Hz. Given that traditional ultrasound operates with refresh rates on the order of 1 kHz, the SLM refresh rate seems quite lacking. However as this study is a proof of concept demonstration (and anticipating near-future SLM hardware advances), this refresh rate is deemed acceptable for the time being. Furthermore, even more limiting is the nanosecond laser's repetition rate of 30 Hz. This again was deemed an acceptable consequence of the development process and plans are in place to procure a laser with a repetition rate more suitable to clinical applications.

Any summary of the future of this technique would be incomplete without discussion of the potential biomedical applications of arbitrary acoustic waveform creation. While the results of the preceding investigation are limited to simple beam steering, the implications of such a versatile ultrasound wavefront generation method are numerous. Utilizing more phase delay enables larger beam steering angles, flexible focus targeting, creating multiple foci, and arbitrary wavefront patterning. Also a topic for future publication is the integration of this ultrasound generation technique with optical detection methods. By utilizing large optical apertures, it is possible to capture a larger 'numerical aperture' worth of Fourier components. And by being optical in nature, the detection Fourier space is also more filled in than compared with traditional transducer detection methods. This shares similarities with photoacoustic tomography and is indeed an attractive avenue for exploration. The large 'transducer count' also lends itself readily to applications in multiple beam scanning: as phased array radar can scan many more beams in space compared to a mechanically-scanned system, so too could the body be scanned by

Biomedical Optics EXPRESS

many beams in parallel [57], speeding large-scale ultrasound mapping and reducing the need for skilled ultrasound technicians to administer the scan. The large aperture would serve to increase the lateral resolution of the projected ultrasound field, allowing beam forming to be used to scan through difficult regions of the body by routing the waves around bones [58] and the lungs. Indeed, the large number of transducers could be used in a similar manner to adaptive optics, correcting wavefront aberrations caused by, say, the skull to create tight ultrasonic foci for focused ultrasound, for example [59]. These extensions of the preceding proof of concept described in this work will enable this technique to be applied to clinical imaging applications showcasing the scalability and flexibility of the novel wavefront generation method.

5.3. Concluding remarks

A new photoacoustic wavefront construction method has been validated experimentally. As a proof of concept of the broader arbitrary wavefront generation method, a photoacoustic beam steering technique has been demonstrated which uses a free-space optical beam delay and SLM-generated holograms to produce an optically-driven acoustic phase ramp on a thermoelastic polymer. The resulting acoustic field was measured at a propagation distance of 20 mm with a steering angle of around 5 degrees, in agreement with Rayleigh-Sommerfeld diffraction principles. The acoustic aperture is highly configurable as is the related phase delay facilitated by the optical delay line. This serves as a verification of a new photoacoustic wavefront generation process, which allows for theoretically arbitrary acoustic phase profiles.

Funding. Engineering and Physical Sciences Research Council (EP/S016538/1, EP/W024969/1, EP/X017842/1); Biotechnology and Biological Sciences Research Council (BB/T011947/1, BB/X004716/1); Wellcome Trust (212490/Z/18/Z); Cancer Research UK (29694, EDDPMA-May22\100059); Royal Society ((RGS\R2\212305, IES\R2\222231); Chan Zuckerberg Initiative (2020-225443, 2020-225707); Imperial College Excellence Fund for Frontier Research.

Disclosures. The authors declare no conflicts of interest.

Data Availability. Data underlying the results presented in this paper are not publicly available at this time but may be obtained from the authors upon reasonable request.

References

1. P. N. T. Wells, "Ultrasound imaging," Phys. Med. Biol. **51**(13), R83–R98 (2006).
2. W. Lee and Y. Roh, "Ultrasonic transducers for medical diagnostic imaging," Biomed. Eng. Lett. **7**(2), 91–97 (2017).
3. Y. Roh, "Ultrasonic transducers for medical volumetric imaging," Jpn. J. Appl. Phys. **53**(7S), 07KA01 (2014).
4. Jin Xuecheng, "The microfabrication of capacitive ultrasonic transducers," J. Microelectromech. Syst. **7**(3), 295–302 (1998).
5. R. Manwar, K. Kratkiewicz, and K. Avanaki, "Overview of Ultrasound Detection Technologies for Photoacoustic Imaging," Micromachines **11**(7), 692 (2020).
6. M. G. Tolsgaard, C. Ringsted, E. Dreisler, *et al.*, "Reliable and valid assessment of ultrasound operator competence in obstetrics and gynecology: Assessment of ultrasound competence," Ultrasound Obstet. & Gynecol. **43**, 437–443 (2014).
7. A. Pinto, F. Pinto, A. Faggian, *et al.*, "Sources of error in emergency ultrasonography," Critical Ultrasound J. **5**(S1), S1 (2013).
8. C. Scruby, "Some applications of laser ultrasound," Ultrasonics **27**(4), 195–209 (1989).
9. S. J. Davies, C. Edwards, G. S. Taylor, *et al.*, "Laser-generated ultrasound: its properties, mechanisms and multifarious applications," J. Phys. D: Appl. Phys. **26**(3), 329–348 (1993).
10. T. Murray, J. Deaton, and J. Wagner, "Experimental evaluation of enhanced generation of ultrasonic waves using an array of laser sources," Ultrasonics **34**(1), 69–77 (1996).
11. M. Clark, S. D. Sharples, and M. G. Somekh, "Diffractive acoustic elements for laser ultrasonics," The J. Acoust. Soc. Am. **107**(6), 3179–3185 (2000).
12. M. D. Brown, J. Jaros, B. T. Cox, *et al.*, "Control of broadband optically generated ultrasound pulses using binary amplitude holograms," The J. Acoust. Soc. Am. **139**(4), 1637–1647 (2016).
13. A. Meyer, S. Gspan, S. Bernet, *et al.*, "Binary optoacoustic holography with a spatial light modulator," J. Appl. Phys. **96**(10), 5886–5891 (2004).
14. S. Gspan, A. Meyer, S. Bernet, *et al.*, "Räumliche und zeitliche Kontrolle über Ultraschallfelder mittels optoakustischer Holographie," Zeitschrift fur Medizinische Phys. **14**(3), 173–179 (2004).
15. F. Schmieder, L. Büttner, and J. Czarske, "Adaptive laser-induced ultrasound generation using a micro-mirror array spatial light modulator," Opt. Express **24**(20), 22536 (2016).

Biomedical Optics EXPRESS

16. T. Wei, H. Guo, J. Lu, *et al.*, "Generating arbitrary photoacoustic fields with a spatial light modulator," Opt. Lett. **44**(13), 3206 (2019).
17. J. S. Steckenrider, T. W. Murray, J. W. Wagner, *et al.*, "Sensitivity enhancement in laser ultrasonics using a versatile laser array system," The J. Acoust. Soc. Am. **97**(1), 273–279 (1995).
18. S. N. Hopko, I. C. Ume, and D. S. Erdahl, "Development of a Flexible Laser Ultrasonic Probe," J. Manuf. Sci. Eng. **124**(2), 351–357 (2002).
19. E. J. Alles, S. Noimark, E. Zhang, *et al.*, "Pencil beam all-optical ultrasound imaging," Biomed. Opt. Express **7**(9), 3696 (2016).
20. N. Huynh, O. Ogunlade, E. Zhang, *et al.*, "Photoacoustic imaging using an 8-beam Fabry-Perot scanner," Proc. SPIE **9708**, 97082L (2016).
21. M. D. Brown, E. Martin, B. T. Cox, *et al.*, "Single pulse illumination of multi-layer photoacoustic holograms for patterned ultrasound field generation," in *2016 IEEE International Ultrasonics Symposium (IUS)*, (IEEE, Tours, France, 2016), pp. 1–4.
22. M. D. Brown, D. I. Nikitichev, B. E. Treeby, *et al.*, "Generating arbitrary ultrasound fields with tailored optoacoustic surface profiles," Appl. Phys. Lett. **110**(9), 094102 (2017).
23. E. J. Alles, R. J Colchester, and A. E. Desjardins, "Adaptive All-Optical Ultrasound Imaging Through Temporal Modulation of Excitation Light," in *2018 IEEE International Ultrasonics Symposium (IUS)*, (IEEE, Kobe, 2018), pp. 1–9.
24. M. D. Brown, "Phase and amplitude modulation with acoustic holograms," Appl. Phys. Lett. **115**(5), 053701 (2019).
25. J. Zhou, N. Wu, and X. Wang, "The enhancement of the photoacoustic generation efficiency based on fiber optic ultrasound phased array," Measurement **146**, 668–674 (2019).
26. M. Basij, Y. Yan, S. S. Alshahrani, *et al.*, "Miniaturized phased-array ultrasound and photoacoustic endoscopic imaging system," Photoacoustics **15**, 100139 (2019).
27. J. Zhou and J. V. Jokerst, "Photoacoustic imaging with fiber optic technology: A review," Photoacoustics **20**, 100211 (2020).
28. D. Thompson, D. Gasteau, and S. Manohar, "Spatially compounded plane wave imaging using a laser-induced ultrasound source," Photoacoustics **18**, 100154 (2020).
29. Y. He, Z. Tang, Z. Chen, *et al.*, "A novel photoacoustic tomography based on a time-resolved technique and an acoustic lens imaging system," Phys. Med. Biol. **51**(10), 2671–2680 (2006).
30. H. W. Baac, J. G. Ok, A. Maxwell, *et al.*, "Carbon-Nanotube Optoacoustic Lens for Focused Ultrasound Generation and High-Precision Targeted Therapy," Sci. Rep. **2**(1), 989 (2012).
31. K. J. Francis, B. Chinni, S. S. Channappayya, *et al.*, "Characterization of lens based photoacoustic imaging system," Photoacoustics **8**, 37–47 (2017).
32. Z. Xu, W. Xu, M. Qian, *et al.*, "A flat acoustic lens to generate a Bessel-like beam," Ultrasonics **80**, 66–71 (2017).
33. K. J. Francis, B. Chinni, S. S. Channappayya, *et al.*, "Multiview spatial compounding using lens-based photoacoustic imaging system," Photoacoustics **13**, 85–94 (2019).
34. M. Chen, L. Jiang, C. Cook, *et al.*, "High-speed wide-field photoacoustic microscopy using a cylindrically focused transparent high-frequency ultrasound transducer," Photoacoustics **28**, 100417 (2022).
35. D. Vella, A. Mrzel, A. Drnovšek, *et al.*, "Ultrasonic photoacoustic emitter of graphene-nanocomposites film on a flexible substrate," Photoacoustics **28**, 100413 (2022).
36. M. D. Brown, B. T. Cox, and B. E. Treeby, "Binary Volume Acoustic Holograms," Phys. Rev. Appl. **19**(4), 044032 (2023).
37. R. J. Mailloux, *Phased array antenna handbook*, Artech House antennas and propagation library (Artech House, Boston, 2005), 2nd ed.
38. J. U. White, "Long Optical Paths of Large Aperture," J. Opt. Soc. Am. **32**(5), 285 (1942).
39. D. Herriott, H. Kogelnik, and R. Kompfner, "Off-Axis Paths in Spherical Mirror Interferometers," Appl. Opt. **3**(4), 523 (1964).
40. R. W. Gerchberg and W. O. Saxton, "A Practical Algorithm for the Determination of Phase from Image and Diffraction Plane Pictures," Optik **35**(2), 237–246 (1972).
41. V. Andreev, A. Karabutov, and A. Oraevsky, "Detection of ultrawide-band ultrasound pulses in optoacoustic tomography," IEEE Trans. Ultrason., Ferroelect., Freq. Contr. **50**(10), 1383–1390 (2003).
42. Y. Hou, J.-S. Kim, S. Ashkenazi, *et al.*, "Optical generation of high frequency ultrasound using two-dimensional gold nanostructure," Appl. Phys. Lett. **89**(9), 093901 (2006).
43. Yang Hou, J.-S. Kim, S.-W. Huang, *et al.*, "Characterization of a broadband all-optical ultrasound transducer-from optical and acoustical properties to imaging," IEEE Trans. Ultrason., Ferroelect., Freq. Contr. **55**(8), 1867–1877 (2008).
44. M. Kalms, S. Hellmers, P. Huke, *et al.*, "Beam shaping using liquid crystal-on-silicon spatial light modulators for laser ultrasound generation," Opt. Eng. **53**(4), 044110 (2014).
45. S. Noimark, R. J. Colchester, B. J. Blackburn, *et al.*, "Carbon-Nanotube-PDMS Composite Coatings on Optical Fibers for All-Optical Ultrasound Imaging," Adv. Funct. Mater. **26**, 8390–8396 (2016).
46. S.-L. Chen, "Review of Laser-Generated Ultrasound Transmitters and Their Applications to All-Optical Ultrasound Transducers and Imaging," Appl. Sci. **7**(1), 25 (2016).

Biomedical Optics EXPRESS

47. B. Dong, C. Sun, and H. F. Zhang, "Optical Detection of Ultrasound in Photoacoustic Imaging," IEEE Trans. Biomed. Eng. **64**(1), 4–15 (2017).
48. T. Zhao, L. Su, and W. Xia, "Optical Ultrasound Generation and Detection for Intravascular Imaging: A Review," J. Healthcare Eng. **2018**, 1–14 (2018).
49. T. Lee, H. W. Baac, Q. Li, *et al.*, "Efficient Photoacoustic Conversion in Optical Nanomaterials and Composites," Adv. Opt. Mater. **6**, 1800491 (2018).
50. S. Noimark, R. J. Colchester, R. K. Poduval, *et al.*, "Polydimethylsiloxane Composites for Optical Ultrasound Generation and Multimodality Imaging," Adv. Funct. Mater. **28**, 1704919 (2018).
51. D. Cui, Z. Zhang, and Y. Shi, "Optically-excited simultaneous photoacoustic and ultrasound imaging based on a flexible gold-PDMS film," J. Innov. Opt. Health Sci. **13**(04), 2050012 (2020).
52. J. Li, J. Xu, X. Liu, *et al.*, "A novel CNTs array-PDMS composite with anisotropic thermal conductivity for optoacoustic transducer applications," Compos. Part B: Eng. **196**, 108073 (2020).
53. X. Zeng and R. J. McGough, "Evaluation of the angular spectrum approach for simulations of near-field pressures," The J. Acoust. Soc. Am. **123**(1), 68–76 (2008).
54. G. Kino, *Acoustic Waves: Devices, Imaging, and Analog Signal Processing*, Prentice-Hall Contemporary Topics in Accounting Series (Prentice-Hall, 1987).
55. M. J. Booth, "Adaptive optics in microscopy," Phil. Trans. R. Soc. A. **365**(1861), 2829–2843 (2007).
56. Z. Gongjian, Z. Man, and Z. Yang, "Wave front control with SLM and simulation of light wave diffraction," Opt. Express **26**(26), 33543 (2018).
57. L. Tong, A. Ramalli, R. Jasaityte, *et al.*, "Multi-Transmit Beam Forming for Fast Cardiac Imaging–Experimental Validation and In Vivo Application," IEEE Trans. Med. Imaging **33**(6), 1205–1219 (2014).
58. J.-F. Aubry, M. Pernot, F. Marquet, *et al.*, "Transcostal high-intensity-focused ultrasound: *ex vivo* adaptive focusing feasibility study," Phys. Med. Biol. **53**(11), 2937–2951 (2008).
59. J.-F. Aubry, M. Tanter, M. Pernot, *et al.*, "Experimental demonstration of noninvasive transskull adaptive focusing based on prior computed tomography scans," The J. Acoust. Soc. Am. **113**(1), 84–93 (2003).

155.198.10.117 {ts '2024-01-03 10:17:51'}